

The Spectral Behaviour and Variability of Narrow-line Seyfert 1 Galaxies with Australia Telescope Compact Array Observations

Xi Shao,^{1,2,3} Philip G. Edwards,^{3*} Jamie Stevens,⁴ Minfeng Gu,¹ Timothy J. Galvin,⁵ and Minh T. Huynh⁵

¹ Shanghai Astronomical Observatory, Chinese Academy of Sciences, 80 Nandan Road, Shanghai 200030, People's Republic of China

² University of Chinese Academy of Sciences, 19A Yuquan Road, Beijing 100049, People's Republic of China

³ CSIRO Space and Astronomy, Australian Telescope National Facility, Epping, New South Wales 1710, Australia

⁴ CSIRO Space and Astronomy, 1828 Yarrrie Lake Road, Narrabri, NSW 2390, Australia

⁵ CSIRO Space and Astronomy, PO Box 1130, Bentley, WA 6102, Australia

Accepted XXX. Received YYY; in original form ZZZ

ABSTRACT

We present multi-frequency radio data for a sample of narrow-line Seyfert 1 galaxies. We first focus on the sub-class of gamma-ray emitting narrow-line Seyfert 1 galaxies, studying the long-term radio variability of five sources and comparing it to their gamma-ray state. We then extend the observations of the southern narrow-line Seyfert 1 galaxy sample of Chen et al. by observing several candidate narrow-line Seyfert 1 sources for the first time, and re-observing several other gamma-ray quiet sources to obtain a first indication of their radio variability. We find that the gamma-ray emitting narrow-line Seyfert 1 galaxies are highly variable radio emitters and that there are instances of contemporaneous flaring activity between the radio and gamma-ray band (PKS 0440–00, PMN J0948+0022 and PKS 1244–255). However, there are also cases of significant radio outbursts without gamma-ray counterparts (PMN J0948+0022 and PKS 2004–447). The five gamma-ray NLS1s favour flat or inverted radio spectra, although the spectral indices vary significantly over time. For the gamma-ray quiet sample, the difference between the previous observations at 5.5 GHz and new ATCA observations indicates that over half of the 14 sources exhibit apparent variability. In contrast to gamma-ray loud sources, gamma-ray quiet objects tend to have steep spectra especially in the lower radio band (887.5–1367.5 MHz), with a number of the variable sources having flatter spectra at higher radio frequencies.

Key words: galaxies: active – galaxies: nuclei – galaxies: Seyfert – radio continuum: galaxies

1 INTRODUCTION

Seyfert galaxies are a class of active galactic nuclei (AGN) that were first identified based on their appearance as otherwise normal galaxies with an abnormally bright central core. Spectroscopically, Seyferts can be subdivided into several sub-types. Type 1 Seyfert galaxies have the widths of permitted emission lines Doppler broadened to $\sim 5000 \text{ km s}^{-1}$ but with forbidden lines much narrower, with widths typically $\sim 500 \text{ km s}^{-1}$. A further sub-class is the narrow-line Seyfert 1 galaxies (NLS1s) that were first described by [Osterbrock & Pogge \(1985\)](#). These have, as their name suggests, somewhat narrower lines from the broad line region ($\text{FWHM}(\text{H}\beta) < 2000 \text{ km s}^{-1}$) and have a ratio of [O III] to H β emission lines of less than 3. They also typically have relatively strong Fe II emission ([Goodrich 1989](#)). These characteristics distinguish NLS1s from broad-line Seyfert 1 (BLS1) galaxies.

In contrast to BLS1s, it is generally the case that NLS1s have smaller supermassive black hole masses, in the range $\sim 10^6 - 10^8 M_{\odot}$ ([Peterson & Wandel 1999](#); [Peterson 2011](#); [Järvelä et al. 2015](#); [Cracco et al. 2016](#)). (However, [Viswanath et al. \(2019\)](#) has found that NLS1s have black hole masses and accretion rates similar to BLS1s.) NLS1s have high Eddington ratios, ranging from 0.1 to 1, and even larger

than 1 in some cases (e.g. [Boroson & Green 1992](#); [Marziani et al. 2018](#); [Tortosa et al. 2022](#)).

The majority of NLS1s are hosted in spiral galaxies, but some are found in disk-like galaxies (e.g. [Järvelä et al. 2018](#); [Olguín-Iglesias et al. 2020](#); [Varglund et al. 2022, 2023](#)) or having elliptical hosts ([D’Ammando et al. 2017, 2018](#)).

The most extensive catalogue of candidate NLS1 galaxies is that compiled by [Paliya et al. \(2024\)](#), based on a decomposition of optical spectra from the Sloan Digital Sky Survey Data Release 17. This catalogue contains 22656 NLS1 galaxies, with a companion catalogue of 52273 broad-line Seyfert 1 (BLS1) galaxies.

At X-ray energies, NLS1s generally show strong flux variability ([Turner et al. 1999](#)) and steeper spectral indices ([Grupe et al. 1998](#); [Leighly 1999](#)) with respect to BLS1s. Many NLS1s have a prominent soft X-ray excess ([Boller et al. 1996](#); [Leighly 1999](#); [Crummy et al. 2006](#); [Zhou et al. 2006](#)), with this characteristic proving to be an effective way of identifying new NLS1s. Possible origins include thermal emission from the accretion disc ([Turner & Pounds 1989](#)), non-thermal emission from the jet ([Sambruna et al. 2000](#)), or the Comptonization of photons from disc or broad-line region (BLR) ([Celotti et al. 2007](#)).

The *Compton Gamma Ray Observatory* did not detect gamma-rays from any known NLS1s, and so it was something of a surprise when *Fermi* detected gamma-rays from PMN J0948+0022 in the first year of the mission ([Abdo et al. 2009](#)). The variability at gamma-ray

* E-mail: Philip.Edwards@csiro.au

energies of PMN J0948+0022, and subsequently detected NLS1s, excluded a possible starburst origin for the gamma-ray photons and confirmed the presence of relativistic jets in these sources (Calderone et al. 2011). Recently, Foschini et al. (2022) have systematically compiled a new sample of gamma-ray emitting jetted AGN from fourth catalogue of gamma-ray point sources produced by the *Fermi* Large Area Telescope (LAT) (Abdollahi et al. 2020). They examined available optical spectra of 2980 gamma-ray point sources to measure redshifts and to confirm or change the original LAT classification. This reclassification resulted in 24 NLS1 confirmed sources or candidates. Foschini et al. (2022) note that although NLS1s lie at the low-luminosity tail of the flat-spectrum radio quasar (FSRQ) distribution, the generally smaller supermassive black hole mass and high accretion rate are key differences, making this sub-class of particular interest. Several sources listed as NLS1s in the Fourth *Fermi*-LAT source catalogue (4FGL) were reclassified by Foschini et al. (2022), and conversely, a number of sources listed as flat-spectrum radio quasars in 4FGL were reclassified by Foschini et al. (2022) as NLS1s.

In Table 1 we list all sources included in the 4FGL catalogue that have been associated with a NLS1. These are considered in detail by Foschini et al. (2022), with the fifth column of the table listing their classification of the source. The final grouping of candidates have been suggested as candidate NLS1s by others (Yao et al. 2015; Berton et al. 2017; Paliya et al. 2018; Yao et al. 2019). (We note that additionally, several sources not listed in 4FGL, and therefore not included in Table 1, have been proposed as gamma-ray NLS1s: including SDSS J0031+0936 (Paiano et al. 2019), FBQS J1102+2239 (Foschini 2011a), TXS 1518+423 (Paliya et al. 2018), and SDSS J1641+3454 (Lähteenmäki et al. 2018).)

Consistent with the inference that variable gamma-ray emitting NLS1 galaxies have jets, the majority of this sub-class display a core-jet morphology on the parsec-scale or kiloparsec-scale (e.g., Lister 2018; D’Ammando 2019; Shao et al. 2023). This branch of NLS1s provide a good chance to study jet evolution at an early stage (e.g., Yao & Komossa 2023).

It is traditional to consider AGN based on their radio loudness, R_L , defined by the flux density ratio of rest-frame 5 GHz and 4400 Å (Kellermann et al. 1989). Most NLS1s are radio quiet (RQ), with $R_L < 10$, or radio silent (RS), with only 5~7% classified as radio loud (RL). However, it has been noted that the usefulness of radio loudness in classifying NLS1s may be limited (e.g. Foschini 2011b; Järvelä et al. 2017; Lister 2018; Berton et al. 2020). However, in general terms, radio-loud NLS1 sources have flat spectra in the 1.4–5 GHz range, with some displaying inverted spectra (e.g., Gu et al. 2015). In contrast, most radio-quiet NLS1 sources have steep spectra, either as a power-law, or curved spectra becoming increasingly steep with increasing frequency (e.g. Chen et al. 2022).

Komossa et al. (2006) found that 35 of the 128 (27%) NLS1s they considered had catalogued radio counterparts, but as noted by Lister (2018), all-sky catalogues are generally not very deep. This was demonstrated by the targeted radio observations of southern NLS1 candidates, which resulted in the detection of 49 of 62 sources (79%) with the Karl G. Jansky Very Large Array (VLA) at 5.5 GHz (Chen et al. 2020) and 42 of 85 (49%) with the Australia Telescope Compact Array (ATCA) at 5.5 and/or 9.0 GHz (Chen et al. 2022), respectively.

In this paper, we explore the spectral behaviour and variability of NLS1s with archival ATCA radio data and new observations. In Section 2 we focus on the sub-class of gamma-ray emitting NLS1s, studying the long-term radio variability of five sources and comparing it to their gamma-ray state. In Section 3 we extend the observations of Chen et al. (2018) by observing several candidate NLS1 sources for the first time, and re-observing several other gamma-ray

quiet sources to obtain a first indication of their radio variability. We discuss the difference between our observing results and the previous observations and the underlying emission mechanism in Section 4. The work is summarised in Section 5. Throughout the paper, we follow the convention $S_\nu \propto \nu^\alpha$ where S is flux density, ν is frequency, and α is the spectral index.

2 GAMMA-RAY LOUD NLS1 GALAXIES

There is long-term ATCA monitoring for five *Fermi* γ -ray sources in Table 1: two established NLS1s (PMN J0948+0022 and PKS 1502+036), two sources classified as NLS1 by Foschini et al. (2022) (PKS 0440–00 and PKS 1244–255) and the candidate NLS1, classified as a misaligned AGN by Foschini et al. (2022), PKS 2004–447.

We compare ATCA multi-frequency light curves (using data primarily from ATCA projects C007 and C1730) with *Fermi* light curves. The ATCA project C007 is an Observatory-led program to monitor several hundred bright AGN at multiple frequencies several times per year so that observers can assess their usefulness as calibrator sources. The C1730 project specifically monitors a smaller number of selected gamma-ray sources at a higher cadence, again at multiple frequencies. Data from both programs is pipeline-processed with the results being made available through the ATCA Calibrator Database¹. Note that the reported errors here are statistical only: systematic errors of up to 5% may also be present at 5.5 and 9 GHz (see, e.g., Tingay et al. 2003), and up to 10% at higher frequencies (where atmospheric opacity effects and antenna pointing become more important).

The *Fermi* data used here is taken from the *Fermi*-LAT Light Curve Repository (LCR) (Abdollahi et al. 2023). The LCR is a database of flux-calibrated light curves for over 1500 sources deemed to be variable in the 10 year *Fermi*-LAT point source (4FGL-DR2) catalogue (Ballet et al. 2020). We have used data binned in 1 week intervals in this paper.

2.0.1 PKS 0440–00

The *Fermi* light curve for PKS 0440–00 in Fig. 1 shows three epochs of enhanced activity, centred on MJD 55000, 56500 and 60200. The radio monitoring is sparse, but it is notable that the highest 5.5 and 9.0 GHz flux densities approximately coincide with the MJD 56500 gamma-ray outburst, and the highest 17, 21 and 33 GHz flux densities precede it. The last epoch of radio monitoring occurred shortly after the MJD 60200 gamma-ray outburst had started: the radio flux densities were not particularly high, but the spectrum had flattened (see §2.2).

2.0.2 PMN J0948+0022

PMN J0948+0022 was the first NLS1 detected by *Fermi*, and the light curve in Fig. 2 shows pronounced activity during the first ~8 years of the mission, and lower level activity until MJD 59000, but relative quiescence thereafter. High cadence radio monitoring over the first years of the *Fermi* mission have been described by Foschini et al. (2012), Angelakis et al. (2015) and Lähteenmäki et al. (2017), with the frequent OVRO monitoring at 15 GHz in particular revealing a series of peaks separated by several months. The ATCA monitoring suggests a peak around MJD 55550, which is confirmed by the works

¹ <https://www.narrabri.atnf.csiro.au/calibrators/>

just cited. The highest 9.0 GHz flux density in the ATCA monitoring at MJD 56450 coincides with a peak seen between 8 and 23 GHz by Angelakis et al. (2015). The next highest 9.0 GHz flux densities occur around MJD 57800, while the source was somewhat less active at gamma-rays. Most notable, however, is a pronounced (and better-sampled) radio flare starting around MJD 59200, which shows the "classical" radio flare characteristics of peaking earlier and higher at higher frequencies, with some evidence for a small secondary peak around MJD 60000. This radio flare however is not accompanied by any significant gamma-ray activity.

2.0.3 PKS 1244–255

The *Fermi* light curve for PKS 1244–255 in Fig. 3 shows a prolonged period of activity from MJD 54700 to MJD 57000, followed by shorter flares around MJDs 58200, 58700 and 59200. The radio monitoring is sparse, but there is a clear doubling in 9.0 GHz flux density between MJD 56000 and MJD 56400, accompanied by a lagging increase in the 5.5 GHz flux densities. (We have excluded one epoch of 7 mm data near MJD 56120, for which the pipelined data analysis had yielded a value above 4 Jy. Inspection of other sources observed close in time at that epoch revealed other unexpectedly high values, and so we have omitted that data point here.) The highest flux densities over the 15 year period occur near MJD 58400, after the MJD 58200 gamma-ray peak. The radio monitoring is particularly infrequent around this time, but the two epochs near MJD 58400 of ATCA monitoring confirm this radio high state. Since that time, the radio flux densities have generally been in a long-term decline, though with an increase coinciding with the MJD 59200 gamma-ray activity. In recent years the gamma-ray activity has been at its lowest level.

2.0.4 PKS 1502+036

The *Fermi* light curve of PKS 1502+036 in Fig. 4 indicates it is the faintest of the sources considered here. Prior to MJD 59600, the sparse radio data peaked around MJD 57400. Somewhat surprisingly, the radio data post MJD 59600 shows a clear peak at 5.5 and 9.0 GHz with the flux densities at 17, 21 and 33 GHz staying almost constant. The 5.5 and 9.0 GHz peak at MJD 60000 comes near the start of the most significant gamma-ray activity in this source.

2.0.5 PKS 2004–447

Although considered as a NLS1 previously (Oshlack et al. 2001), Foschini et al. (2022) label PKS 2004–447 a misaligned jetted AGN. Berton et al. (2021) confirm that the optical spectrum meets the classification of an NLS1, but propose that the source is a hybrid Compact Steep Spectrum (CSS)/NLS1, based on its radio properties, noting that these hybrid characteristics are similar to 3C 286. The *Fermi* light curve in Fig. 5 reveals that the source is largely quiescent, being detected in only 20% of one-week bins, with the exception being a prominent gamma-ray flare in 2019. Gokus et al. (2021) made a multi-wavelength examination of data around this time, and report significant increases in optical/UV fluxes coincident with the flare. The gamma-ray flare occurred during a several-year period of gradually increasing radio flux densities, but did not result in any dramatic short-term radio outburst. More recently, as revealed by Fig. 5, there has been a pronounced radio flare, with frequencies between 5.5 and 21 GHz increasing simultaneously over ~6 months from MJD 59840. The higher frequencies then decline more rapidly

than lower frequencies, with a secondary radio peak around MJD 60200. These are the highest flux densities over the 10 years in the 1 cm band, however, the radio flare is not accompanied by any appreciable activity at gamma-ray energies.

2.1 Variability indices

We follow Tingay et al. (2003) in calculating a radio variability index, defined as the rms variation about the mean, divided by the mean flux density, in each band for each source. Tingay et al. (2003) studied 185 radio-loud (5 GHz flux density $> \sim 1$ Jy) AGN over a 3.5-year period in the 1.4, 2.5, 4.8 and 8.4 GHz bands. That study yielded median variability indices in those bands of 0.06, 0.06, 0.08 and 0.09 respectively, with 90% of sources having variability indices below 0.20, 0.20, 0.24 and 0.28. It is apparent from Table 2 that the five gamma-ray loud NLS1 sources we have studied all have variability indices generally well in excess of these median values, and PMN J0948+0022 and PKS 1244–255 have variabilities in the top 10% of the Tingay et al. (2003) sample. This is consistent with the finding of Tingay et al. (2003) that gamma-ray loud AGN (i.e., at that time, EGRET-detected AGN) tended to have higher variability indices than gamma-ray quiet AGN.

2.2 Spectral variation

A detailed wide-band study of the variation in spectra in the preceding radio light curves is complicated by the fact there are only few epochs with simultaneous broad-band data points. Nevertheless, there are enough epochs with observations in at least four bands to make an examination of the range of variations seen in spectra. In Fig. 6, we show spectra at two epochs for each of the five sources considered in the preceding sections. The two epochs have been selected in an attempt to show the extremes of the spectral indices. The values of the spectral indices are tabulated in Table 3. Several features are apparent: while several spectra can be reasonably approximated by a single spectral index over a wide range, more often there is a range of spectral indices present at a single epoch. The difference between flattest and steepest spectral indices in this comparison of two epochs for a given source ranges from 0.49 for PKS 0440–00 to 1.28 for PMN J0948+0022 and PKS 1502+036. Not surprisingly, this range of variation in spectral index results in some sources having steep ($\alpha \leq -0.5$) spectra at some epochs but flat spectra at others. Clearly, for variable sources such as these, care must be taken in obtaining contemporaneous flux densities for any meaningful spectral index studies.

Additionally in Fig. 6 we show a single epoch spectrum between 5.5 and 34 GHz for the candidate NLS1 source TXS 0943+105 (considered as a FSRQ by Foschini et al. (2022)) for comparison with future observations. Examination of the *Fermi*-LAT LCR indicates this source was in a less active gamma-ray state at this epoch, with fewer detections on one-week timescales, compared to the first ~8 years of the *Fermi* mission.

3 GAMMA-RAY QUIET NLS1 GALAXIES

Chen et al. (2018) presented a catalogue of Southern Hemisphere NLS1s derived from the Six-degree Field Galaxy Survey (6dFGS) final data release, classifying 167 NLS1s by their optical spectral properties. Chen et al. (2020) used the VLA in C-configuration to observe 62 of these sources with declinations $> -25^\circ$ at 5 GHz with an image sensitivity of $\sim 7 \mu\text{Jy}$. Subsequently, Chen et al. (2022)

observed 85 of these sources (with declination $< -25^\circ$) at 5.5 and 9.0 GHz with the ATCA. As the VLA is more sensitive, and the observation times were similar, the VLA observations had a higher detection rate than the ATCA observations, as described in Section 1.

As a pilot survey for a potential larger program, we selected 21 sources from the sample of [Chen et al. \(2018\)](#) for observations in ATCA Director's Discretionary Time under the observing code CX540. These sources are listed in Table 4. Ten of the sources had been observed by [Chen et al. \(2020\)](#) and five by [Chen et al. \(2022\)](#), and our observations were intended to determine whether these sources showed evidence of variability at radio frequencies. The other six sources were among 21 sources which were not able to be observed as part of the [Chen et al. \(2020\)](#) VLA sample.

We also collect data from the Rapid ASKAP Continuum Surveys at 887.5 MHz ([Hale et al. 2021](#), RACS-Low) and 1367.5 MHz ([Duchesne et al. 2023](#), RACS-Mid) for our sample. RACS-Low covers the south of a declination of $+41$ degrees, with a median RMS noise level in images of 0.25 mJy/beam. RACS-Mid covers the sky south of a declination of $+49$ degrees, with Stokes I images having a median noise level of 0.20 mJy/beam.

Due to the low flux density of our targets, observations (using project code CX540) were made with 10~15 minute snapshots bracketed by 2-minute scans on a nearby phase calibrator. The ATCA primary flux density calibrator, PKS 1934–638, was also used for bandpass calibration. Data reduction was carried out in MIRIAD ([Sault et al. 1995](#)) using standard procedures. During the calibration, radio frequency interference (RFI) was flagged. Flux densities were measured using the miriad task "imfit".

3.1 Results

Of our sample of 21 sources, we detected 14 sources with the ATCA at 5.5 GHz, with 10 sources also detected at 9.0 GHz. We measured the integrated flux densities of the detected sources and set upper limits of three times the rms noise level for the non-detections. Note again that the reported errors are statistical only: systematic errors of up to 5% may also be present (see, e.g. [Tingay et al. 2003](#)). Fifteen of the 21 sources were matched in RACS-Low, and 16 in RACS-Mid.

With these flux densities we can examine the spectra of these sources. We calculate the spectral index, α , between bands as,

$$\alpha = \frac{\log(S_{\nu_1}/S_{\nu_2})}{\log(\nu_1/\nu_2)}, \quad (1)$$

where S_{ν_1} and S_{ν_2} are the flux densities at frequencies ν_1 and ν_2 , respectively. The error in α is derived following the propagation of errors. We follow the usual convention of categorizing the spectrum as "steep" if $\alpha \leq -0.5$ and "flat" if $\alpha > -0.5$. Fourteen of the 15 sources detected in both RACS surveys have steep spectra between 887.5 and 1367.5 MHz (given as α_1 in Table 4). Between 1367.5 MHz and 5.5 GHz, twelve sources have a steep spectrum and four targets show a flat spectra (α_2). Finally, between 5.5 and 9.0 GHz, eight sources have steep spectra while six sources have flat spectra (α_3).

The medians of α_1 , α_2 and α_3 are -1.0 ± 0.5 , -0.9 ± -0.0 and 0.0 ± 0.3 , respectively. Details of spectral indices are displayed in Table 4 and the overall distribution of the spectral index types of our sample is depicted in Fig. 7 including the sources with upper limits showing obvious spectral type. Note that we observed two sources, J1500–7248 and J1515–7820, twice: we take the data observed on 2024 February 17 for the spectral index calculation due to their longer integration times. The potential mechanisms result in various spectral index will be discussed in Section 4.

3.1.1 Sources previously observed with the VLA

We observed ten sources selected from [Chen et al. \(2020\)](#) which were detected by VLA at 5.5 GHz. All ten sources were detected in both RACS-Low and RACS-Mid. We detected six of these sources at both 5.5 and 9.0 GHz, and three at only 5.5 GHz. As expected, the ATCA non-detections were generally the faintest of the [Chen et al. \(2020\)](#) detections. The main reason for re-examining these sources was to search for evidence of radio variability among these gamma-ray quiet NLS1s, and several sources have varied significantly over the ~5 years between the VLA observations and our ATCA observations, most notably J0122–2646 (from 0.9 to 7.1 mJy), J0452–2953 (from 3.4 to 0.7 mJy) and J0447–0508 (from 4.0 to 2.4 mJy). (We note that for J0447–0508, Table 4 lists integrated flux densities of 89.0 mJy for RACS-Low yet only 8.2 mJy for RACS-Mid. RACS-Mid resolves this source into two distinct components, yet with the lower angular resolution of RACS-Low, they appear as a single extended source.)

3.1.2 Sources previously observed with the ATCA

Five sources had previously been observed with the ATCA by [Chen et al. \(2022\)](#). The brighter sources show strong variability: J1057–4089 (from 168 to 283 mJy at 5.5 GHz and from 152 to 301 mJy at 9.0 GHz) and J1500–7248 (from 31 mJy to 54 and 79 mJy at 5.5 GHz and from 35 mJy to 60 mJy at 9.0 GHz in the two epochs we observed it). We note that [Chen et al. \(2022\)](#) find these two sources both show significant structure, which could potentially result in flux density not being fully recovered in short snapshot observations (if the position angle of the synthesized differs significantly from that of the source structure). However, the [Chen et al. \(2022\)](#) observations were made in a 750m array, whereas our observations, which yielded higher flux densities, were made in 6 km arrays, suggesting resolution effects are unlikely to be a significant factor in this case.

J0609–5606 was a faint detection previously (0.4 mJy) but was not re-detected. J0307–7250 was of particular interest as it had previously been detected at 9.0 GHz but not 5.5 GHz. We did not detect it at either frequency, and note further that the source is not listed in either of the RACS catalogues. However, our upper limit at 9.0 GHz is only just below the reported flux density of [Chen et al. \(2022\)](#). At face value, these facts suggest a (possibly variable) inverted spectrum source, which merits further follow-up. J1515–7820 is the only source that shows different spectral types in 4 cm band in two slots, as the flux density at 9.0 GHz significantly decreased while that at 5.5 GHz remained the same.

3.1.3 Sources not previously observed

As [Chen et al. \(2020\)](#) were not able to observe all sources with declinations $> -25^\circ$, there are 13 sources in the original observing catalogue ([Chen et al. 2018](#)) that are not considered in the final paper. We observed six of these sources (J0133–2109, J2137–1112, J2229–1401, J2244–1822, J2250–1152 and J2311–2022) for relatively short integrations, mostly 20 minutes. One source, J2250–1152, was detected at both 5.5 and 9.0 GHz, and another, J2229–1401, was detected at 5.5 GHz only. It is noteworthy that neither of these sources were detected in the RACS-Low or RACS-Mid surveys, despite simple extrapolations from the ATCA detections suggesting the RACS-band flux densities would be well above the respective noise levels. This suggests that either the spectra are more complex, or that the sources have varied significant over the intervening two years, or both.

4 DISCUSSION

4.1 The variabilities

Archival multi-frequency ATCA radio data has allowed the radio state of five gamma-ray loud NLS1s to be compared to their gamma-ray state, as indicated by data from the *Fermi*-LAT LCR. The *Fermi* LCR data reveals a wide range in activity levels of detected NLS1s: PKS 1244–255 was detected in 73% of the weekly-binned data, whereas PKS 0221+067 and GB6 J1102+5249 were only detected 6% of the time (Table 1). The radio variability indices for the five sources we considered are generally well above the median variabilities determined for a sample of radio-loud AGN by Tingay et al. (2003). Although the cadence of our radio data is limited, particularly for the early years of the *Fermi* mission, we are still able to draw a number of conclusions. There are peaks in our radio light curves that are consistent with those previously reported (Foschini et al. 2012; Angelakis et al. 2015; Lähteenmäki et al. 2017). In some cases radio flares are contemporaneous with gamma-ray outbursts, e.g., PKS 0440–003 in 2014, PMN J0948+0022 in 2010 and 2013 and PKS 1244–255 in 2021.

The sparsity of the radio monitoring, and the fact that gamma-ray active states can continue for many years, preclude any conclusions on time lags between gamma-ray and radio activity. However, it is evident that radio outbursts are not necessarily proportionate to gamma-ray activity: the under-sampled 2018 radio flare in PKS 1244–255 follows a small increase in gamma-ray flux, whereas five years of similar gamma-ray activity at the start of the *Fermi* mission coincided with more modest radio variability.

There are also several examples of pronounced radio outbursts which are not accompanied by any perceptible change in gamma-ray state, e.g., the 2021 flare in PMN J0048+0022, and the 2022 flare in PKS 2004–447. Similar behaviour has been reported for other sources (e.g. Lähteenmäki & Valtaoja 2003). Perhaps most surprising is the 2022 flare seen at 5.5 and 9.0 GHz for PKS 1502+036, which does not appear to have a counterpart at higher radio frequencies. Angelakis et al. (2015) note the occurrence of radio flares which "disappear" below some frequency in the cm-band, but we are not aware of flares disappearing above some cutoff.

Foschini et al. (2012) note the variability of gamma-ray and radio fluxes from PMN J0948+0022 in 2009 and 2010 followed the canonical expectations of relativistic jets, with gamma-rays leading the radio emission by a few months, but that the multi-frequency behaviour was less clear in 2011. In particular, they note an "orphan" optical/X-ray flare in October 2011 with no counterpart at gamma-ray energies. D'Ammando et al. (2014) also examine the multi-wavelength behaviour of PMN J0948+0022 in 2011, noting that variability observed in optical and near-infrared in April/May has no counterpart at gamma-ray energies. They suggest this behaviour could be related to a bending and inhomogeneous jet, possibly containing a turbulent multi-cell structure.

A key goal for our study of a gamma-ray quiet sample of NLS1s was to determine whether this class also showed evidence for variability at 5.5 GHz. This class of sources also tends to be much fainter at radio wavelengths, with longer integrations required to detect (sub-)mJy-level sources. Comparison of our measured flux densities with those of Chen et al. (2020) and Chen et al. (2022) revealed clear evidence of variability ($> 3\sigma$) for over half of the 14 sources detected at two epochs over the several year period between observations. (And there are another three undetected sources whose variations between two epochs exceed 3σ in their statistical errors.) We acknowledge that the effects of differing angular resolutions, incomplete (u, v) coverages, and different primary flux density calibrators between the VLA

and ATCA may contribute to apparent variability, for the fainter sources in particular, however it is incontrovertible that a number of these gamma-ray quiet NLS1s show significant radio variability. At face value, this might be seen as evidence in favour of jetted radio emission over a predominantly star formation (SF) origin in these variable sources, however a more definitive test would be with follow-up VLBI observations of these sources (cf Gu et al. 2015; Lister 2018; Shao et al. 2023).

4.2 The spectral behaviour

For the five gamma-ray loud NLS1s for which we have multi-epoch multi-frequency data, we were able to compare the spectral behaviour at two contrasting epochs. These confirmed that these gamma-ray and radio-loud sources tend to have flat or inverted radio spectra at most epochs, though the actual value of the spectral index can vary significantly. This highlights that contemporaneous flux density measurements are required for any meaningful spectral index studies of such variable sources. There are a few cases where the flux densities exceed 2 Jy at multiple frequencies (with inverted spectra), such as PMN J0948+0022 and PKS 1244–255, indicating that the dominant contribution is from the relativistic jet (especially for PMN J0948+0022, which displays a parsec-scale jet morphology) rather than SF.

In contrast, the gamma-ray quiet sample tend to have steep spectra. We combined RACS-Low (887.5 MHz) and RACS-Mid (1367.5 MHz) data with our 5.5 and 9 GHz data, to determine up to three spectral indices. A number of sources had steep ($\alpha < -0.5$) spectra across this whole frequency range. No source had flat spectra between all frequencies, though a number of sources had flat spectra at the higher frequencies, where the median spectral index was 0.0 ± 0.3 (see Table 4 there was a tendency for the more variable sources to have flatter spectra, but also exceptions to this trend (such as J1044–1826)).

Spectra, like variability, can also provide clues as to the origin of the radio emission. Radio spectra can be made up of contributions from SF, relativistic jets, accretion disk corona, AGN-driven winds or outflows, free-free emission (FFE) and even external Compton processes. Diffuse emission is widely observed in the SF radio morphology on the host galaxy scale with optically thin spectra from several hundred MHz to ~ 10 GHz following $\alpha = -0.8 \pm 0.4$ (Gim et al. 2019; An et al. 2021) without apparent spectral breaks or turnover. Jet and wind contributions are difficult to distinguish based on the spectra and morphology, as both can launch pc to kpc linear structures (Berton et al. 2018; Chen et al. 2020; Yao et al. 2021) but the spectra would be expected to be steeper if extended emission dominates, or flatter if a compact core dominates. For radio emission from the corona, the morphology would be compact and optically thick on sub-pc scales, requiring VLBI observations to determine whether the jet base has high brightness temperature and whether the radio emission is collimated or not. A spectral index of -0.1 would be expected if FFE dominates. Of our sample, only J1057–4039 approached this value, with $\alpha_2 = -0.1 \pm 0.0$. Three of our sources might have spectra close to expectations for a SF dominated case: J0122–2646 has $\alpha_1 = -0.8 \pm 0.8$, J0400–2500 has $\alpha_2 = -0.8 \pm 0.2$ and J0447–0508 has $\alpha_3 = -0.8 \pm 0.4$.

However, these consistencies in only specific frequency intervals can't be taken as the conclusive evidence of the emission mechanism, as the models predict spectral indices over broader frequency ranges. Therefore, the emission mechanism in our gamma-ray quiet NLS1s remains unclear, with further studies required.

5 CONCLUSION

In this paper we have studied two classes of NLS1 galaxies. For a sample of five gamma-ray loud NLS1s, we have compared the ~ 16 year gamma-ray light curves from *Fermi* with archival multi-frequency radio monitoring with the ATCA between 2.1 and 33 GHz. Although the radio data is sparse, particular in the early years, a number of conclusions can be drawn.

- These variable gamma-ray sources are also highly variable radio sources.
- Radio flares can in some instances be associated with gamma-ray high states.
- There are also significant radio flares with no corresponding increase in gamma-ray activity.

We have extended the study of candidate gamma-ray quiet NLS1 galaxies from the sample of [Chen et al. \(2018\)](#) with new ATCA observation and added ASKAP survey data as well. As a pilot survey for a potential larger program, we selected 21 sources, ten of which had been detected with the VLA by [Chen et al. \(2020\)](#), five of which had been detected with the ATCA by [Chen et al. \(2022\)](#), and six of which had not been previously observed at 5.5 GHz. We compiled data from the ASKAP RACS-Low and RACS-Mid surveys around 1 GHz for these sources and calculated the spectral indices.

- About half of the 14 sources detected at two epochs showed evidence of radio variability.
- Although the spectra between 887.5 MHz and 9.0 GHz were generally steep, a number of sources, and preferentially the variable sources, had flat spectra at the higher frequencies (1367.5 MHz–5.5 GHz and 5.5–9.0 GHz).
- Two of six sources previously not observed at 5.5 GHz were detected for the first time.

While illuminating, the under-sampled nature of the archival ATCA light curves results in our comparison with gamma-ray light curves being qualitative rather than quantitative. As stressed by other workers (e.g., [Foschini et al. 2012](#); [Yao & Komossa 2023](#)) higher cadence multi-frequency monitoring is required to obtain data sets amenable to detailed SED modelling. We plan to continue higher cadence multi-frequency monitoring of the gamma-ray loud sources with the ATCA.

ACKNOWLEDGEMENTS

We give great thanks to the referee for comments which have improved the paper. XS is grateful for the support from CSIRO and the SKA PhD scholarship from China Scholarship Council. The Australia Telescope Compact Array is part of the Australia Telescope National Facility (<https://ror.org/05qajvd42>) which is funded by the Australian Government for operation as a National Facility managed by CSIRO. We acknowledge the Gomeri people as the Traditional Owners of the Observatory site.

XS and MFG are supported by the National Science Foundation of China (grant 12473019), the National SKA Program of China (Grant No. 2022SKA0120102), the Shanghai Pilot Program for Basic Research-Chinese Academy of Science, Shanghai Branch (JCYJ-SHFY-2021-013), and the China Manned Space Project with No. CMSCSST-2021-A06.

DATA AVAILABILITY

The ATCA data used in this paper is available in the Australia Telescope Online Archive (ATOA) at <https://atoa.atnf.csiro.au> with project codes of CX540, C007 and C1730.

Table 1. *Fermi* detected NLS1s based on Foschini et al. (2022).

Catalogue name (1)	<i>Fermi</i> Name (2)	z (3)	Class _{original} (4)	Class _{revised} (5)	$N_{\text{detection}}$ (6)	$N_{\text{upper limit}}$ (7)	$R_{\text{detection}}$ (8)	Ph_{highest} (9)	$Ave(F_{5.5\text{GHz}})$ (10)
IH 0323+342	J0324.8+3412	0.063	nlsy1	NLS1	203	612	0.25	9.58E-07	0.350 ± 0.005
SBS 0846+513	J0850.0+5108	0.584	NLSY1	NLS1	177	644	0.22	4.19E-07	
PMN J0948+0022	J0948.9+0022	0.584	NLSY1	NLS1	423	380	0.53	7.34E-07	0.266 ± 0.001
IERS B1303+515	J1305.3+5118	0.785	nlsy1	NLS1					
B3 1441+476	J1443.1+4728	0.703	nlsy1	NLS1					
PKS 1502+036	J1505.0+0326	0.408	NLSY1	NLS1	324	478	0.40	3.66E-07	0.741 ± 0.002
MG2 J164443+2618	J1644.9+2620	0.144	NLSY1	NLS1	87	736	0.11	2.98E-07	
revised class									
PKS 2004–447	J2007.9-4432	0.24	nlsy1	MIS	164	662	0.20	7.54E-07	0.429 ± 0.001
TXS 2116–077	J2118.8-0723c	0.26	nlsy1	SEY					0.103 ± 0.003
new classified									
TXS 2358+209	J0001.5+2113	0.439	fsrq	NLS1	259	564	0.31	9.04E-07	
GB6 J0102+4214	J0102.4+4214	0.874	fsrq	NLS1	100	720	0.12	1.59E-07	
PKS 0221+067	J0224.2+0700	0.511	fsrq	NLS1	52	773	0.06	2.80E-07	
PKS 0440–00	J0442.6-0017	0.844	fsrq	NLS1	464	361	0.56	1.47E-06	2.449 ± 0.005
S4 0929+53	J0932.6+5306	0.597	fsrq	NLS1	108	712	0.13	4.04E-05	
3C 232	J0958.0+3222	0.531	fsrq	NLS1					
PKS 1045–18	J1048.0-1912	0.595	fsrq	NLS1					
GB6 J1102+5249	J1102.6+5251	0.69	fsrq	NLS1	49	773	0.06	1.17E-07	
B3 1151+408	J1154.0+4037	0.923	fsrq	NLS1	91	730	0.11	1.73E-07	
PKS 1200–051	J1202.5-0528	0.381	fsrq	NLS1	119	706	0.14	2.74E-07	
TXS 1206+549	J1208.9+5441	1.34	fsrq	NLS1	299	523	0.36	3.80E-07	
PKS B1211–190	J1214.6-1926	0.149	bcu	NLS1					
PKS 1244–255	J1246.7-2548	0.638	fsrq	NLS1	601	220	0.73	1.58E-06	1.153 ± 0.002
TXS 1308+554	J1310.9+5514	0.926	fsrq	NLS1					
TXS 1700+685	J1700.0+6830	0.301	fsrq	NLS1	466	353	0.57	1.00E-06	
MG1 J181841+0903	J1818.6+0903	0.354	fsrq	NLS1	122	701	0.15	1.91E-07	
B2 1846+32A	J1848.4+3217	0.798	fsrq	NLS1	210	613	0.26	8.68E-07	
candidates									
GB6 J0937+5008*	J0937.1+5008	0.28	fsrq	SEY					
TXS 0943+105*	J0946.6+1016	1.00	fsrq	FSRQ	352	465	0.43	2.82E-07	0.345 ± 0.004
OK 290	J0956.7+2516	0.71	fsrq	FSRQ					
4C +04.42*	J1222.5+0414	0.97	fsrq	FSRQ					
3C 286*	J1331.0+3032	0.85	css	MIS					
TXS 1419+391	J1421.1+3859	0.49	fsrq	FSRQ					
PMN J2118+0013*	J2118.0+0019	0.46	fsrq	SEY					

Notes. Column (1): source names in catalogues (those marked with * are sources already known as blazars or/and γ -ray emitters); column(2): source names in *Fermi*-4FGL catalogue; column (3): redshifts from Foschini et al. (2022); column (4-5): original and revised classification in Foschini et al. (2022) where nlsy1 and NLSY1 represent firmly associated narrow-line Seyfert 1 galaxy and nlsy1 an associated narrow-line Seyfert 1 galaxy with lower confidence; NLS1 is narrow-line Seyfert 1 galaxy, fsrq and FSRQ represent flat-spectrum radio quasar, bcu represents the unclassified source, CSS, MIS and SEY represent compact steep-spectrum source, misaligned AGN and Seyfert galaxy, respectively; column (6-7): the numbers of *Fermi* detections and upper limits in the weekly-binned *Fermi* LAT Light Curve Repository, respectively; column (8): the detection rate calculated by $N_{\text{detection}} / (N_{\text{detection}} + N_{\text{upper limit}})$; column (9): the highest photon fluxes detected by *Fermi*-LAT in the unit of $0.1 - 100 \text{ GeV ph cm}^{-2} \text{ s}^{-1}$; column (10): the mean of flux densities at 5.5 GHz (long-term ATCA data) in the unit of Jy.

Table 2. The radio variability indices of *Fermi* detected γ -ray NLS1s.

Catalogue name (1)	Source (2)	2100 MHz		5500 MHz		9000 MHz		17000 MHz		21000 MHz		33000 MHz	
		N (3)	m (4)	N (5)	m (6)	N (7)	m (8)	N (9)	m (10)	N (11)	m (12)	N (13)	m (14)
PKS 0440–00	0440–003	3	0.08 ± 0.06	9	0.25 ± 0.00	9	0.23 ± 0.01	20	0.25 ± 0.01	20	0.24 ± 0.01	17	0.30 ± 0.03
PMN J0948+0022	0946+006	18	0.46 ± 0.16	33	0.44 ± 0.03	33	0.50 ± 0.02	12	0.37 ± 0.05	12	0.39 ± 0.05	11	0.43 ± 0.03
PKS 1244–255	1244–255	14	0.26 ± 0.03	38	0.40 ± 0.01	38	0.49 ± 0.01	15	0.49 ± 0.01	15	0.52 ± 0.01	10	0.63 ± 0.02
PKS 1502+036	1502+036	4	0.29 ± 0.07	18	0.21 ± 0.01	18	0.22 ± 0.01	13	0.15 ± 0.02	13	0.16 ± 0.03	17	0.18 ± 0.04
PKS 2004–447	2004–447	11	0.13 ± 0.02	114	0.14 ± 0.02	114	0.17 ± 0.04	76	0.28 ± 0.07	76	0.32 ± 0.08	44	0.24 ± 0.13

Notes. Column (1) source name in catalogues; column (2) is source name in project C007; column (3, 5, 7, 9, 11, 13) are the numbers of ATCA observations at each frequency, column (4, 6, 8, 10, 12, 14) are the radio variability index of each light curve, calculated as the rms about the mean, divided by the mean flux density.

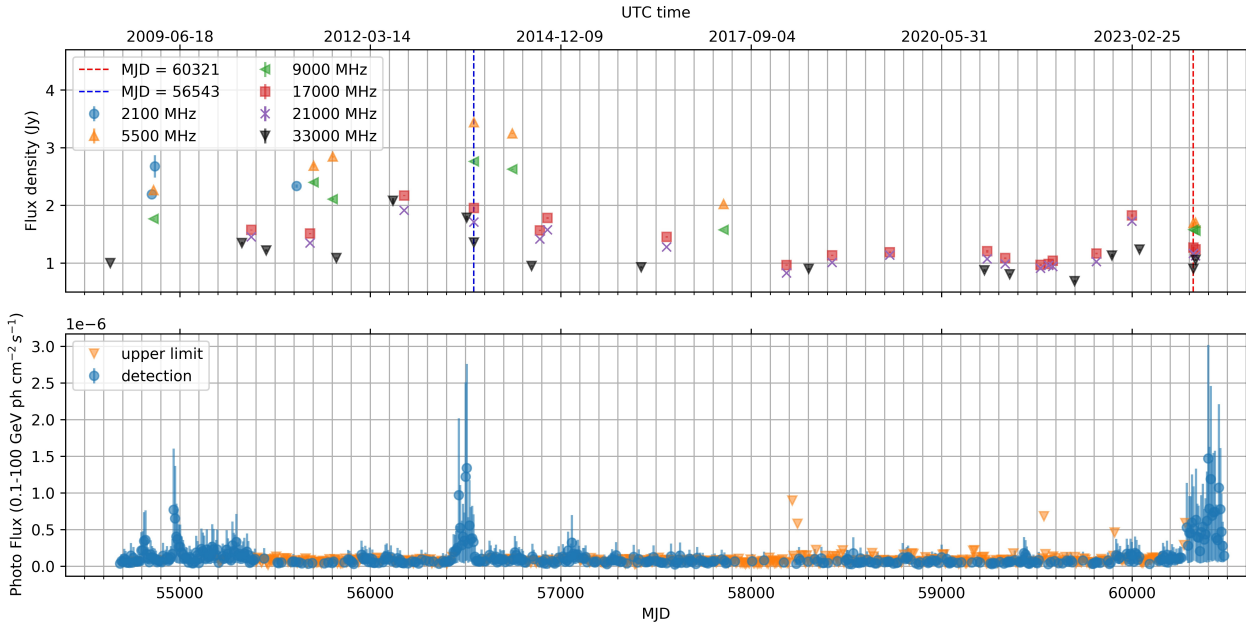


Figure 1. The radio and gamma-ray light curves of PKS 0440–00. The dashed lines indicate the epochs for which radio spectra are shown in Figure 6.

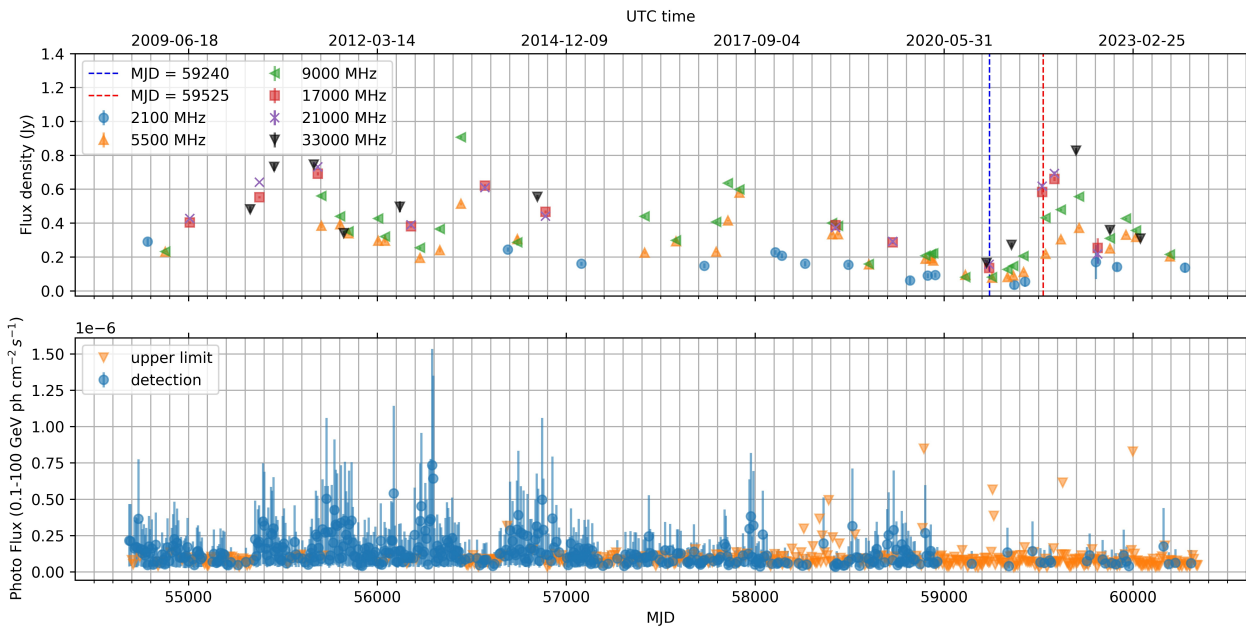


Figure 2. The radio and gamma-ray light curves of PMN J0948+0022. The dashed lines indicate the epochs for which radio spectra are shown in Figure 6.

REFERENCES

- Abdo A. A., et al., 2009, *ApJ*, 699, 976
 Abdollahi S., et al., 2020, *ApJS*, 247, 33
 Abdollahi S., et al., 2023, *ApJS*, 265, 31
 An F., et al., 2021, *MNRAS*, 507, 2643
 Angelakis E., et al., 2015, *A&A*, 575, A55
 Ballet J., Burnett T. H., Digel S. W., Lott B., 2020, *arXiv e-prints*, p. [arXiv:2005.11208](https://arxiv.org/abs/2005.11208)
 Berton M., et al., 2017, *Frontiers in Astronomy and Space Sciences*, 4, 8
 Berton M., et al., 2018, *A&A*, 614, A87
 Berton M., et al., 2020, *A&A*, 636, A64
 Berton M., et al., 2021, *A&A*, 654, A125
 Boller T., Brandt W. N., Fink H., 1996, *A&A*, 305, 53
 Boroson T. A., Green R. F., 1992, *ApJS*, 80, 109
 Calderone G., Foschini L., Ghisellini G., Colpi M., Maraschi L., Tavecchio F., Decarli R., Tagliaferri G., 2011, *MNRAS*, 413, 2365
 Celotti A., Ghisellini G., Fabian A. C., 2007, *MNRAS*, 375, 417
 Chen S., et al., 2018, *A&A*, 615, A167
 Chen S., et al., 2020, *MNRAS*, 498, 1278
 Chen S., et al., 2022, *MNRAS*, 512, 471
 Cracco V., Ciroi S., Berton M., Di Mille F., Foschini L., La Mura G., Rafanelli P., 2016, *MNRAS*, 462, 1256

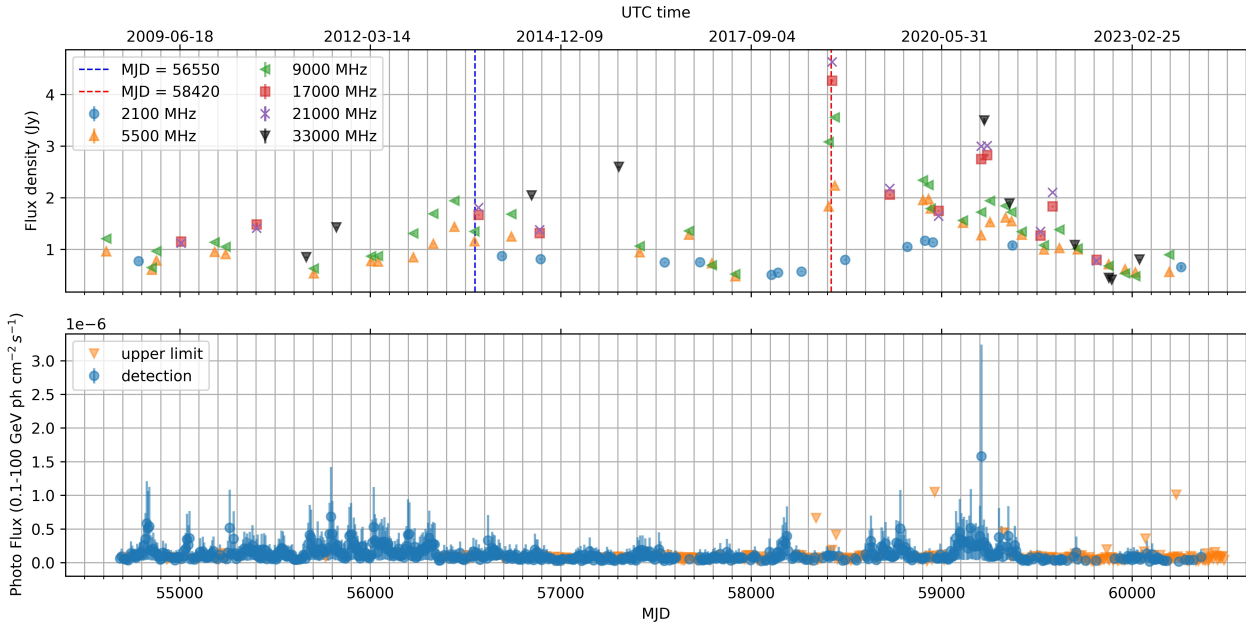


Figure 3. The radio and gamma-ray light curves of PKS 1244–255. The dashed lines indicate the epochs for which radio spectra are shown in Figure 6.

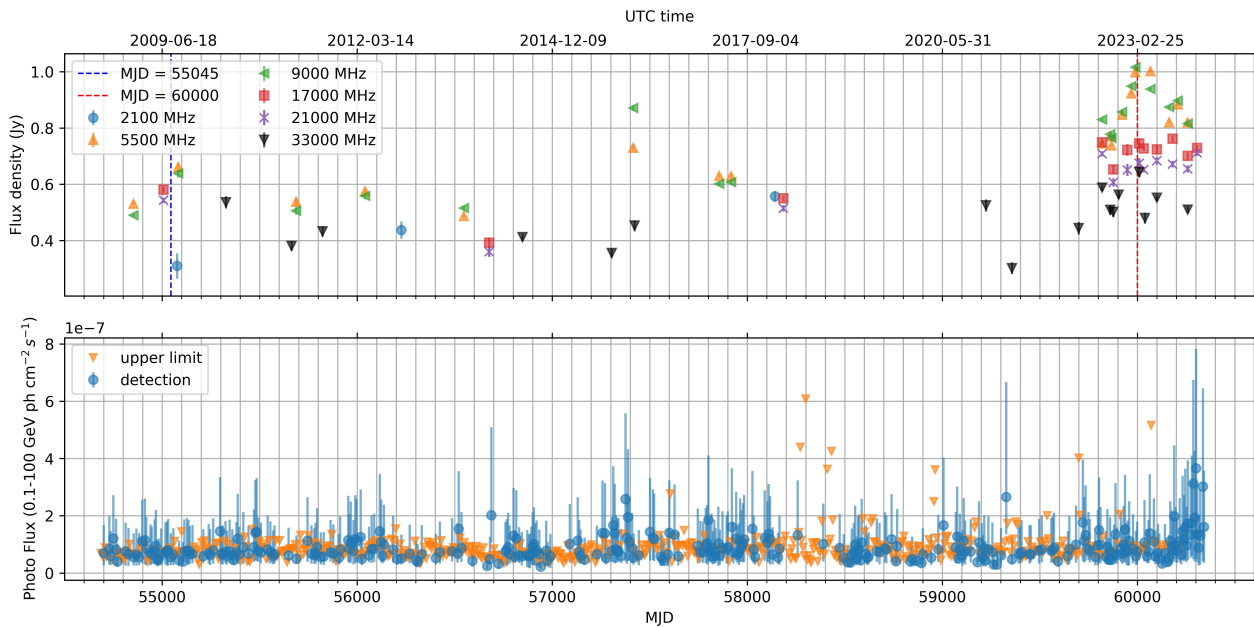


Figure 4. The radio and gamma-ray light curves of PKS 1502+036. The dashed lines indicate the epochs for which radio spectra are shown in Figure 6.

Crummy J., Fabian A. C., Gallo L., Ross R. R., 2006, *MNRAS*, **365**, 1067
D’Ammando F., 2019, *Galaxies*, **7**, 87
D’Ammando F., et al., 2014, *MNRAS*, **438**, 3521
D’Ammando F., Acosta-Pulido J. A., Capetti A., Raiteri C. M., Baldi R. D., Orienti M., Ramos Almeida C., 2017, *MNRAS*, **469**, L11
D’Ammando F., Acosta-Pulido J. A., Capetti A., Baldi R. D., Orienti M., Raiteri C. M., Ramos Almeida C., 2018, *MNRAS*, **478**, L66
Duchesne S. W., et al., 2023, *Publ. Astron. Soc. Australia*, **40**, e034
Foschini L., 2011a, in Foschini L., Colpi M., Gallo L., Grupe D., Komossa S., Leighly K., Mathur S., eds, *Narrow-Line Seyfert 1 Galaxies and their Place in the Universe*. p. 24 (arXiv:1105.0772),

doi:10.22323/1.126.0024
Foschini L., 2011b, *Research in Astronomy and Astrophysics*, **11**, 1266
Foschini L., et al., 2012, *A&A*, **548**, A106
Foschini L., et al., 2022, *Universe*, **8**, 587
Gim H. B., et al., 2019, *ApJ*, **875**, 80
Gokus A., et al., 2021, *A&A*, **649**, A77
Goodrich R. W., 1989, *ApJ*, **342**, 224
Grupe D., Beuermann K., Thomas H. C., Mannheim K., Fink H. H., 1998, *A&A*, **330**, 25
Gu M., Chen Y., Komossa S., Yuan W., Shen Z., Wajima K., Zhou H., Zensus J. A., 2015, *ApJS*, **221**, 3

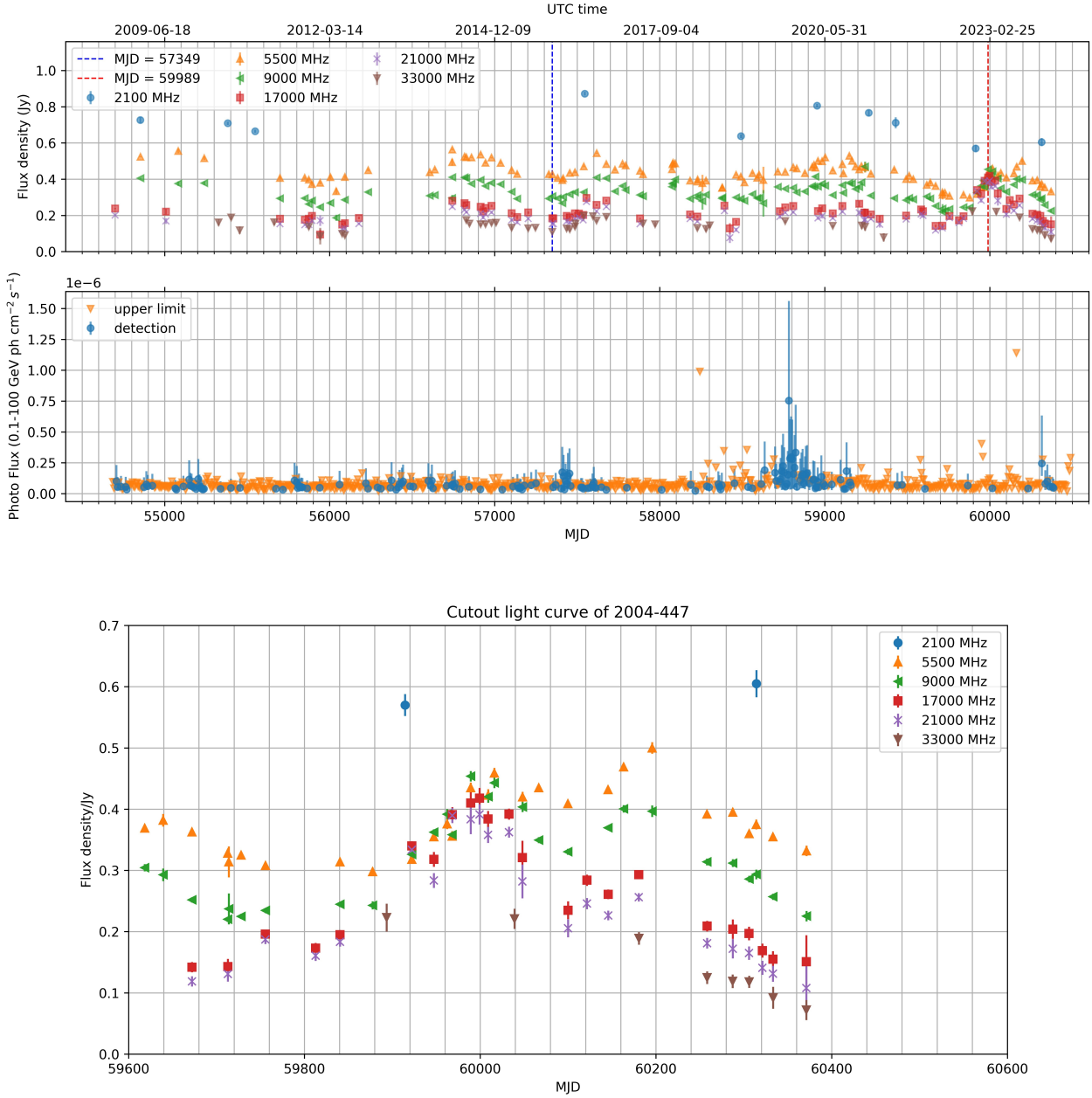


Figure 5. The radio and gamma-ray light curves of PKS 2004–447. The dashed lines indicate the epochs for which radio spectra are shown in Figure 6. The bottom panel is an expanded view of the radio flare starting around MJD 59900.

Hale C. L., et al., 2021, *Publ. Astron. Soc. Australia*, **38**, e058

Järvelä E., Lähteenmäki A., León-Tavares J., 2015, *A&A*, **573**, A76

Järvelä E., Lähteenmäki A., Lietzen H., Poudel A., Heinämäki P., Einasto M., 2017, *A&A*, **606**, A9

Järvelä E., Lähteenmäki A., Berton M., 2018, *A&A*, **619**, A69

Kellermann K. I., Sramek R., Schmidt M., Shaffer D. B., Green R., 1989, *AJ*, **98**, 1195

Komossa S., Voges W., Xu D., Mathur S., Adorf H.-M., Lemson G., Duschl W. J., Grupe D., 2006, *AJ*, **132**, 531

Lähteenmäki A., Valtaoja E., 2003, *ApJ*, **590**, 95

Lähteenmäki A., et al., 2017, *A&A*, **603**, A100

Lähteenmäki A., Järvelä E., Ramakrishnan V., Tornikoski M., Tammi J., Vera R. J. C., Chamani W., 2018, *A&A*, **614**, L1

Leighly K. M., 1999, *ApJS*, **125**, 317

Lister M., 2018, in *Revisiting Narrow-Line Seyfert 1 Galaxies and their Place in the Universe*. p. 22 ([arXiv:1805.05258](https://arxiv.org/abs/1805.05258)), doi:10.22323/1.328.0022

Marziani P., et al., 2018, *Frontiers in Astronomy and Space Sciences*, **5**, 6

Olguín-Iglesias A., Kotilainen J., Chavushyan V., 2020, *MNRAS*, **492**, 1450

Oshlack A. Y. K. N., Webster R. L., Whiting M. T., 2001, *ApJ*, **558**, 578

Osterbrock D. E., Pogge R. W., 1985, *ApJ*, **297**, 166

Paiano S., Falomo R., Treves A., Franceschini A., Scarpa R., 2019, *ApJ*, **871**, 162

Paliya V. S., Ajello M., Rakshit S., Mandal A. K., Stalin C. S., Kaur A., Hartmann D., 2018, *ApJ*, **853**, L2

Paliya V. S., Stalin C. S., Domínguez A., Saikia D. J., 2024, *MNRAS*, **527**, 7055

Peterson B. M., 2011, *arXiv e-prints*, p. [arXiv:1109.4181](https://arxiv.org/abs/1109.4181)

Peterson B. M., Wandel A., 1999, *ApJ*, **521**, L95

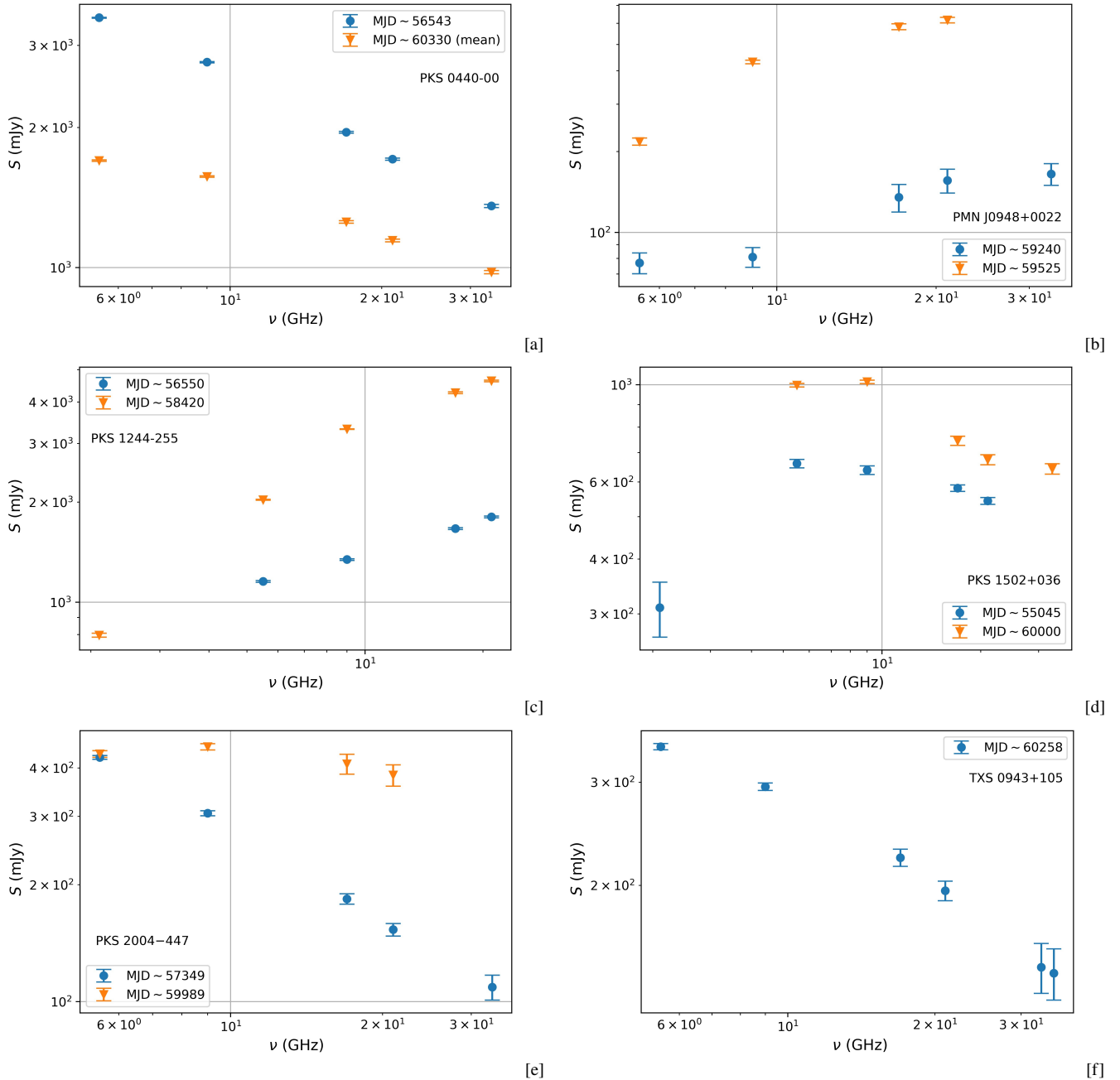


Figure 6. Panel [a] to [e] are the spectra for the two epochs indicated in Figures 1 to 5 for PKS 0440–00, PMN J0948+0022, PKS 1244–255, PKS 1502+036, and PKS 2004–447, respectively. Panel [f] is the single epoch spectrum for TXS 0943+105.

Sambruna R. M., Chou L. L., Urry C. M., 2000, *ApJ*, **533**, 650
 Sault R. J., Teuben P. J., Wright M. C. H., 1995, in Shaw R. A., Payne H. E., Hayes J. J. E., eds, *Astronomical Society of the Pacific Conference Series Vol. 77, Astronomical Data Analysis Software and Systems IV*. p. 433 ([arXiv:astro-ph/0612759](https://arxiv.org/abs/astro-ph/0612759)), doi:10.48550/arXiv.astro-ph/0612759
 Shao X., Gu M., Chen Y., Yang H., Yao S., Yuan W., Shen Z., 2023, *ApJ*, **943**, 136
 Tingay S. J., Jauncey D. L., King E. A., Tzioumis A. K., Lovell J. E. J., Edwards P. G., 2003, *PASJ*, **55**, 351
 Tortosa A., et al., 2022, *MNRAS*, **509**, 3599
 Turner T. J., Pounds K. A., 1989, *MNRAS*, **240**, 833
 Turner T. J., George I. M., Netzer H., 1999, *ApJ*, **526**, 52
 Varglund I., Järvelä E., Lähteenmäki A., Berton M., Ciroi S., Congiu E., 2022, *A&A*, **668**, A91

Varglund I., Järvelä E., Ciroi S., Berton M., Congiu E., Lähteenmäki A., Di Mille F., 2023, *A&A*, **679**, A32
 Viswanath G., Stalin C. S., Rakshit S., Kurian K. S., Ujjwal K., Gudennavar S. B., Kartha S. S., 2019, *ApJ*, **881**, L24
 Yao S., Komossa S., 2023, *MNRAS*, **523**, 441
 Yao S., Yuan W., Zhou H., Komossa S., Zhang J., Qiao E., Liu B., 2015, *MNRAS*, **454**, L16
 Yao S., Komossa S., Liu W.-J., Yi W., Yuan W., Zhou H., Wu X.-B., 2019, *MNRAS*, **487**, L40
 Yao S., et al., 2021, *MNRAS*, **508**, 1305
 Zhou H., Wang T., Yuan W., Lu H., Dong X., Wang J., Lu Y., 2006, *ApJS*, **166**, 128

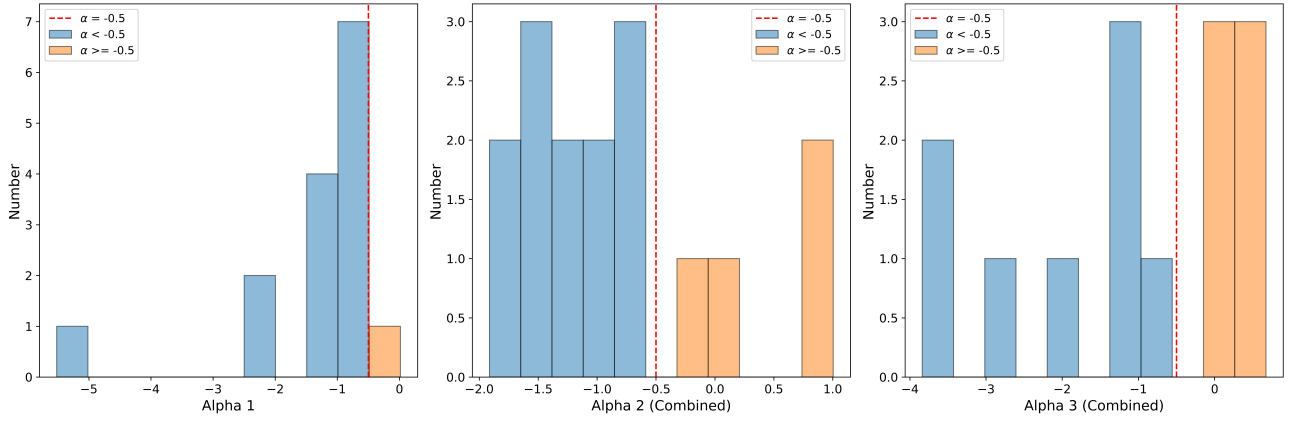


Figure 7. The histogram of the spectral indices for gamma-ray quiet sources in the [Chen et al. \(2020, 2022\)](#) sample. The left panel (α_1) is the spectral index between RACS-Low (887.5 MHz) and RACS-Mid (1367.5 MHz). The central panel (α_2) is the spectral index between RACS-Mid and 5.5 GHz. The right panel (α_3) is the spectral index between 5.5 and 9.0 GHz (the observation of J1515–7820 on 2024 Feb 17 was selected) and the "combined" in x-axis presents the data including the upper limits on the spectral index.

Table 3. The spectral indices of γ -ray NLS1s, from the epochs shown in Figures 1 to 5.

Catalogue name (1)	Source (2)	MJD (3)	α_1 (4)	α_2 (5)	α_3 (6)	α_4 (7)	α_5 (8)
PKS 0440–00	0440–003	56543		-0.45 ± 0.01	-0.54 ± 0.01	-0.63 ± 0.03	-0.51 ± 0.02
		60321		-0.14 ± 0.01	-0.34 ± 0.02	-0.41 ± 0.07	-0.57 ± 0.04
PMN J0948+0022	0946+006	59240		0.10 ± 0.25	0.80 ± 0.23	0.69 ± 0.74	0.12 ± 0.31
		59525		1.38 ± 0.07	0.48 ± 0.05	0.27 ± 0.17	
PKS 1244–255	1244–255	56550		0.31 ± 0.02	0.34 ± 0.01	0.38 ± 0.04	
		58420	0.97 ± 0.01	0.99 ± 0.01	0.40 ± 0.01	0.39 ± 0.04	
PKS 1502+036	1502+036	55045	0.79 ± 0.15	-0.07 ± 0.06	-0.15 ± 0.04	-0.32 ± 0.12	
		60000		0.04 ± 0.03	-0.49 ± 0.04	-0.47 ± 0.17	-0.11 ± 0.09
PKS 2004–447	2004–447	57349		-0.67 ± 0.04	-0.80 ± 0.05	-0.86 ± 0.23	-0.75 ± 0.18
		59989		0.09 ± 0.06	-0.16 ± 0.10	-0.32 ± 0.41	

Notes. Column (1) source name in catalogues; column (2) is source names in project C007; column (3) are MJD time of epochs; column (4–8) are the in-band spectral index between 2.1 and 5.5 GHz, between 5.5 and 9.0 GHz, between 9.0 and 17 GHz, between 17 and 21 GHz and between 21 and 33 GHz, respectively.

This paper has been typeset from a \LaTeX file prepared by the author.

Table 4. Flux densities and spectral indices of NLS1s.

Name	RA (h:m:s)	Dec (d:m:s)	z	$F_{887.5\text{ MHz}}$ (mJy)	$F_{1367.5\text{ MHz}}$ (mJy)	Ep	T (min)	$F_{5.5\text{ GHz}}$ (mJy)	$F_{9.0\text{ GHz}}$ (mJy)	$S_{5.5\text{ GHz}}$ (mJy)	$S_{9.0\text{ GHz}}$ (mJy)	α_1	α_2	α_3	Note
(1)	(2)	(3)	(4)	(5)	(6)	(7)	(8)	(9)	(10)	(11)	(12)	(13)	(14)	(15)	(16)
J0122–2646	01:22:37.52	-26:46:45.9	0.417	2.8 ± 0.9	2.0 ± 0.3	D	30	7.1 ± 0.2	1.1 ± 0.3	0.9 ± 0.1 ^v	-	-0.8 ± 0.8	0.9 ± 0.1	-3.8 ± 0.7	SFS
J0133–2109	01:33:35.03	-21:09:59.0	0.130	3.5 ± 0.5	2.3 ± 0.4	B	20	<0.3	<0.3	-	-	-1.0 ± 0.5	<-1.4	-	SS-
J0230–0859	02:30:05.53	-08:59:53.20	0.016	4.7 ± 0.6	3.2 ± 0.4	F	45	0.6 ± 0.1	<0.3	1.2 ± 0.0 ^v	-	-0.9 ± 0.4	-1.2 ± 0.2	<-1.3	SSS
J0307–7250	03:07:35.32	-72:50:02.50	0.028	-	-	B	30	<0.3	<0.3	<0.1 ^a	0.4 ± 0.03 ^a	-	-	-	-
J0354–1340	03:54:32.85	-13:40:07.29	0.076	18.1 ± 1.3	6.6 ± 0.5	D	30	7.0 ± 0.1	8.9 ± 0.0	5.1 ± 0.0 ^v	-	-2.3 ± 0.2	0.0 ± 0.1	0.5 ± 0.0	SFF
J0400–2500	04:00:24.42	-25:00:44.48	0.097	4.0 ± 0.4	2.3 ± 0.3	D	30	0.7 ± 0.2	<0.3	1.2 ± 0.0 ^v	-	-1.2 ± 0.4	-0.8 ± 0.2	<-2.0	SFF
J0422–1854	04:22:56.58	-18:54:41.39	0.064	4.3 ± 0.7	1.7 ± 0.2	F	45	0.7 ± 0.2	<0.4	1.1 ± 0.0 ^v	-	-2.1 ± 0.5	-0.6 ± 0.2	<-1.3	SSS
J0436–1022	04:36:22.32	-10:22:33.23	0.036	21.2 ± 1.0	21.3 ± 2.1	D	30	4.1 ± 0.3	2.1 ± 0.1	4.6 ± 0.2 ^v	-	0.0 ± 0.2	-1.2 ± 0.1	-1.3 ± 0.2	FSS
J0447–0508	04:47:20.72	-05:08:13.99	0.045	89.0 ± 6.8	8.2 ± 0.6	F	45	2.4 ± 0.2	1.6 ± 0.3	4.0 ± 0.1 ^v	-	-5.5 ± 0.3	-0.9 ± 0.1	-0.8 ± 0.4	SSS
J0452–2953	04:52:30.13	-29:53:35.59	0.247	19.1 ± 1.2	10.2 ± 0.7	D	30	0.7 ± 0.1	0.9 ± 0.1	3.4 ± 0.0 ^v	-	-1.4 ± 0.2	-1.9 ± 0.1	0.6 ± 0.4	SSF
J0549–2425	05:49:14.89	-24:25:51.50	0.045	5.1 ± 0.6	3.7 ± 0.4	F	45	<0.5	<0.2	1.6 ± 0.0 ^v	-	-0.7 ± 0.4	<-1.4	-	SS-
J0609–5606	06:09:17.48	-56:06:58.40	0.032	4.1 ± 0.5	3.1 ± 0.3	B	30	<0.3	<0.3	0.4 ± 0.0 ^a	<0.12 ^a	-	-0.7 ± 0.4	-	SS-
J1044–1826	10:44:48.70	-18:26:51.53	0.113	6.8 ± 0.7	5.4 ± 0.6	E	45	1.4 ± 0.2	1.9 ± 0.1	1.6 ± 0.0 ^v	-	-0.5 ± 0.4	-1.0 ± 0.1	0.7 ± 0.4	SSF
J1057–4039	10:57:27.87	-40:39:40.60	0.398	475.4 ± 2.5	309.2 ± 18.6	E	30	282.6 ± 0.1	301.2 ± 0.1	167.7 ± 0.1 ^a	151.7 ± 0.07 ^a	-1.0 ± 0.1	-0.1 ± 0.0	0.1 ± 0.0	SFF
J1500–7248	15:00:12.81	-72:48:40.30	0.141	16.8 ± 0.4	13.4 ± 0.9	E	30	54.1 ± 0.1	60.1 ± 0.1	31.4 ± 0.0 ^a	35.4 ± 0.04 ^a	-0.5 ± 0.2	1.0 ± 0.0	0.2 ± 0.0	SFF
J1500–7248	15:00:12.81	-72:48:40.30	0.141	16.8 ± 0.4	13.4 ± 0.9	A	5	78.7 ± 0.1	76.9 ± 0.1	31.4 ± 0.0 ^a	35.4 ± 0.04 ^a	-0.5 ± 0.2	1.3 ± 0.0	0.0 ± 0.0	SFF
J1515–7820	15:15:15.20	-78:20:12.00	0.259	25.1 ± 0.5	16.3 ± 1.0	E	30	1.8 ± 0.6	1.8 ± 0.1	3.9 ± 0.0 ^a	2.1 ± 0.03 ^a	-1.0 ± 0.2	-1.6 ± 0.2	0.0 ± 0.7	SSF
J1515–7820	15:15:15.20	-78:20:12.00	0.259	25.1 ± 0.5	16.3 ± 1.0	A	5	1.2 ± 0.3	0.7 ± 0.2	3.9 ± 0.0 ^a	2.1 ± 0.03 ^a	-1.0 ± 0.2	-1.9 ± 0.2	-1.1 ± 0.7	SSS
J2137–1112	21:37:47.95	-11:12:03.60	0.113	-	0.9 ± 0.3	B	20	<0.3	<0.2	-	-	-	<-0.7	-	-S-
J2229–1401	22:29:03.51	-14:01:06.20	0.236	-	-	C	20	2.2 ± 0.1	<0.4	-	-	-	-	<-3.6	-S
J2244–1822	22:44:58.19	-18:22:49.50	0.198	-	-	C	20	<0.6	<0.4	-	-	-	-	-	-
J2250–1152	22:50:14.06	-11:52:00.80	0.118	-	-	C	20	4.2 ± 0.1	1.0 ± 0.4	-	-	-	-	-3.0 ± 0.8	-S
J2311–2022	23:11:03.26	-20:22:20.60	0.121	-	-	C	30	<0.3	<0.4	-	-	-	-	-	-
Median	-	-	0.113	6.8 ± 0.7	4.6 ± 0.4	-	30	2.3 ± 0.1	1.9 ± 0.1	3.4 ± 0.0	18.8 ± 0.0	-1.0 ± 0.5	-0.9 ± 0.0	0.0 ± 0.3	-

Notes. Column (1): source names; column (2-3): the coordinate of sources; column (4): redshifts from NED (<http://ned.ipac.caltech.edu/>); column (5-6): flux densities at 887.5 MHz (RACS-Low); and at 1367.5 MHz (RACS-Mid), respectively; column (7): code of epochs, letter A, B, C, D, E and F represent the observations on Dec 3, 2023 and Jan 5, 2024 with 6D Array, on Jan 12 and Jan 25, 2024 with EW367 Array, and Feb 17 and Feb 28, 2024 with 6A Array, respectively; column (8): exposure time; column (9-10): flux densities at 5.5 GHz (ATCA) and 9.0 GHz (ATCA), column (11-12): previous flux densities; superscript letter ^a represents from ATCA observations in 4cm band (Chen et al. 2022) and superscript letter ^v represents from VLA observations at 5.5 GHz (Chen et al. 2020); Columns (13-15): in-band spectral indices between 887.5 MHz and 1367.5 MHz, between 1367.5 MHz and 5.5 GHz (new data), and between 5.5 GHz (new data) and 9.0 GHz (new data), respectively; column(16): spectral types of α_1 , α_2 and α_3 , respectively. The last line gives the median of flux densities and in-band spectral indices at different bands, for sources J1500–7248 and J1515–7820 we select the longer integrated time (30 mins) for the median calculation.